UC Santa Barbara
UC Santa Barbara Previously Published Works

Title

Sub-hertz fundamental linewidth photonic integrated Brillouin laser

Permalink

https://escholarship.org/uc/item/4qk9d4jg

Journal

Nature Photonics, 13(1)

ISSN

1749-4885

Authors

Gundavarapu, Sarat

Brodnik, Grant M

Puckett, Matthew

et al.

Publication Date

2019

DOI

10.1038/s41566-018-0313-2

Sub-hertz fundamental linewidth photonic integrated Brillouin laser

Sarat Gundavarapu [1], Grant M. Brodnik[1], Matthew Puckett[2], Taran Huffman[1], Debapam Bose[1],
Ryan Behunin[3], Jianfeng Wu[2], Tiequn Qiu[2], Cátia Pinho[4], Nitesh Chauhan[1], Jim Nohava[5],
Peter T. Rakich[6], Karl D. Nelson[5], Mary Salit[5] and Daniel J. Blumenthal [1]*

Spectrally pure lasers, the heart of precision high-end scientific and commercial applications, are poised to make the leap from the laboratory to integrated circuits. Translating this performance to integrated photonics will dramatically reduce cost and footprint for applications such as ultrahigh capacity fibre and data centre networks, atomic clocks and sensing. Despite the numerous applications, integrated lasers currently suffer from large linewidth. Brillouin lasers, with their unique properties, offer an intriguing solution, yet bringing their performance to integrated platforms has remained elusive. Here, we demonstrate a sub-hertz (~0.7 Hz) fundamental linewidth Brillouin laser in an integrated Si_3N_4 waveguide platform that translates advantages of non-integrated designs to the chip scale. This silicon-foundry-compatible design supports low loss from 405 to 2,350 nm and can be integrated with other components. Single- and multiple-frequency output operation provides a versatile low phase-noise solution. We highlight this by demonstrating an optical gyroscope and a low-phase-noise photonic oscillator.

Photonic integrated sub-hertz linewidth lasers will enable systems-on-chip solutions for a wide range of high-end and commercial applications, including coherent communications[1], next-generation data centre networks, atomic and quantum sensing[2,3], and atomic clocks[4]. Translating the performance of these spectrally pure lasers to wafer-scale integrated devices will bring lower cost, size, weight and power along with increased environmental robustness to applications that, today, are relegated to the laboratory scale. In addition, an integration platform that supports operation across the visible to infrared (~405 to 2,350 nm) will provide a versatile spectrally pure optical source solution. For example, atomic clocks, the most precise timing references available today, utilize visible wavelength ultralow linewidths obtained by locking a laser to a table-top stabilized, ultralow expansion, high-finesse optical cavity enclosed in vacuum[5,6]. Laser-cooled strontium atom clocks[7] achieve an astounding stability on the order of one part in 10^{17} over a period of 113 h (ref. [8]) by relying on stabilized benchtop laser systems. Sub-hertz linewidth lasers locked to optical transitions in single Yb^+ ions and self-referenced optical frequency combs[9] achieve a fractional frequency noise approaching 10^{-19} by counting microwave output frequencies[10]. Other applications include microwave frequency synthesizers[11], optical laser gyros[12] and modern data centres that leverage atomic clocks for database and transaction synchronization such as Google SPANNER and TrueTime[13]. These same technologies can bring high-capacity coherent wavelength division multiplexed (WDM) fibre links[14] to the data centre network[15,16] and address the exploding optical interconnect capacity[17] that today consumes 10% of global electricity production[18].

The stimulated Brillouin scattering laser[19] is an intriguing class of laser that can produce highly coherent, spectrally pure emission[20,21] and can be designed to operate from the visible[22] to the infrared[23]. Brillouin lasers have a unique property in that they can narrow the pump laser linewidth by many orders of magnitude[21],

producing a low white-frequency-noise floor, low close-to-carrier frequency noise[24] and low relative intensity noise (RIN)[25,26]. The low fundamental linewidth[27], determined by the white-frequency-noise floor, in combination with decreased close-to-carrier frequency noise make the Brillouin laser an important candidate for integrated high-spectral-purity sources. In contrast, today's state of the art monolithic semiconductor[28] and hybrid designs[29] are at best capable of sub-kilohertz fundamental linewidth emission. Discrete component Brillouin lasers with sub-hertz fundamental linewidth emission have been demonstrated[23,30,31]. In particular, fibre Brillouin lasers provide the highest spectral-purity emission due to their large mode-volume, large effective optical mode area, as well as amenability to cavity stabilization, feedback and control techniques for noise reduction.

However, translating the advantages of fibre Brillouin lasers to a truly waveguide integrated platform has remained elusive. Compact chip-scale discrete component Brillouin lasers have utilized etched-silica microdisk[31] and fluoride[30] resonators. Yet these designs present significant challenges with respect to stability, sensitivity to environment conditions, operation across wide wavelength ranges, integration with feedback control actuators and elements, and large noise due to thermo-refractive fluctuations, and are not compatible with low-cost wafer-scale integration processes. Waveguide-based photonic integrated Brillouin lasers have been demonstrated in silicon[32] and chalcogenide platforms[33,34] producing emission linewidths in the 10–100 kHz regime.

Here, we report the demonstration of a sub-hertz (~0.7 Hz) fundamental linewidth all-waveguide photonic integrated laser. The laser is fabricated in a monolithic ultralow-loss silicon nitride (Si_3N_4) platform[35] in a bus–ring waveguide resonator with ~28 million loaded quality factor $Q_L = \omega\tau$, where ω is the photon angular frequency and τ is the cavity photon lifetime. The Brillouin gain is derived from long lifetime photons that continually generate short-lived

[1]Department of Electrical and Computer Engineering, University of California Santa Barbara, Santa Barbara, CA, USA. [2]Honeywell International, Phoenix, AZ, USA. [3]Department of Physics and Astronomy, Northern Arizona University, Flagstaff, AZ, USA. [4]Instituto de Telecomunicações (IT), University of Aveiro, Aveiro, Portugal. [5]Honeywell International, Plymouth, MN, USA. [6]Department of Applied Physics, Yale University, New Haven, CT, USA.
*e-mail: danb@ucsb.edu

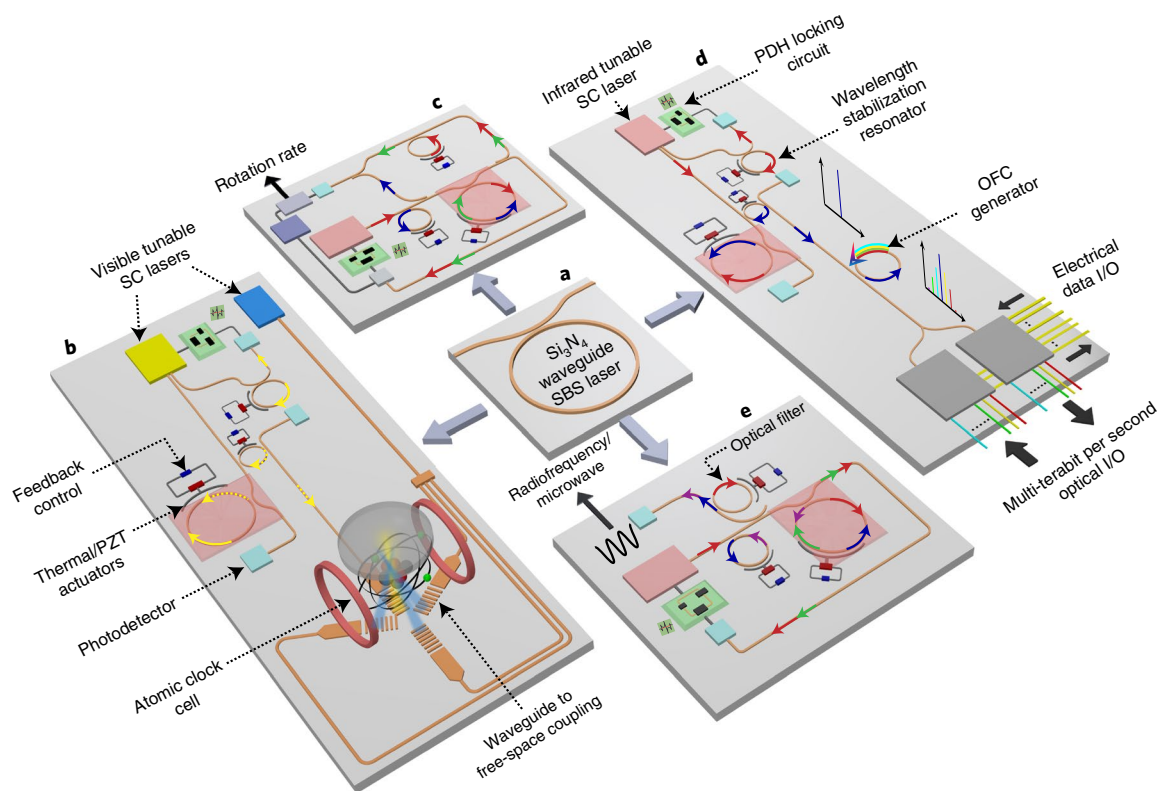**Fig. 1 | Si₃N₄ waveguide Brillouin laser and application system-on-chip examples. a**, Si_3N_4 waveguide stimulated Brillouin scattering (SBS) laser. **b**, Chip-scale atomic clock showing an atomic cell probed by a visible Si_3N_4 waveguide Brillouin laser. The Brillouin laser is pumped by a visible tunable semiconductor (SC) laser. The solid and dashed yellow arrows denote the Brillouin pump and the first Stokes order emission, respectively. The blue SC laser is used to cool the atoms. **c**, Integrated laser optical gyroscope to detect rotation rate based on the Sagnac-induced phase shift between counter-propagating Stokes orders. The red, blue and green arrows denote the Brillouin pump and the first and second Stokes order emission, respectively. **d**, WDM multi-terabit per second coherent transceiver using a Si_3N_4 waveguide Brillouin laser-pumped Si_3N_4 Kerr optical frequency comb (OFC) generator and a multi-channel integrated coherent silicon photonics transceiver. The red and blue arrows denote the Brillouin pump and the first Stokes order emission, respectively. The multi-coloured arrow denotes the OFC generator output. **e**, Low-noise, chip-scale photonic microwave synthesizer that generates microwave frequencies by photo-mixing the highly coherent optical Stokes frequencies emitted from a cascaded-order Si_3N_4 waveguide Brillouin laser. The red, blue, green and purple arrows denote the SBS pump and the first, second and third Stokes orders, respectively. I/O, input/output; PDH, Pound–Drever–Hall; PZT, piezoelectric transducer.

phonons along the optical waveguide path. We leverage this unique property to obtain a broadened gain bandwidth of 153 MHz. Brillouin lasing is demonstrated through measurement of a clear threshold as a function of pump power, linewidth narrowing at the lasing transition, and measurements of the spectral power below, near and above the threshold. The gain, threshold, linewidth and slope efficiency are compared with, and are in strong agreement with, detailed gain simulations and steady-state behaviour modelled using a cascaded-order Brillouin laser dynamics theory[26]. The laser RIN is characterized as a function of pump power and measured to be –150 dBc Hz⁻¹ at 40 MHz frequency offset and the fundamental linewidth corresponds to a white-noise-frequency floor of 0.23 Hz² Hz⁻¹. Our laser brings advantages of fibre and microrod Brillouin lasers to an integrated level. These advantages include a high Q, a large mode-volume, the ability to support high optical intensities and a large mode field area, resulting in noise properties comparable to discrete component dual-cavity microresonator Brillouin lasers[36]. The laser is fabricated using a wafer-scale process involving a single Si_3N_4 etch followed by plasma-enhanced chemical vapour-deposited silicon dioxide upper cladding. This process is fully compatible with a wide range of already demonstrated active and passive devices[37–39] and offers the capability to integrate devices with a range of Q and confinement factors[40,41]. The Brillouin laser, shown in Fig. 1a, is illustrated with four system-on-chip

applications (Fig. 1b–e), highlighting the advantage of low waveguide loss in the 405–2,350 nm wavelength range[39].

Results

Laser design and operating principles. Sub-hertz fundamental linewidth emission is generated through nonlinear photon–phonon coupling within a large-mode-volume, high-Q, monolithic integrated Si_3N_4 waveguide bus-coupled ring resonator (Fig. 2a). The laser resonator supports optical modes at the Brillouin frequencies of the pump and the Stokes fields and can be run in single-frequency or cascaded-order multiple-frequency output operation. The relations between optical cavity resonances, Brillouin frequency shift and gain profile, and the optical pump and the first Stokes order (S1) are illustrated in Fig. 2b (not to scale). In lasing, S1 (red curve) is frequency downshifted from the pump (blue curve) by the Brillouin frequency offset, $\Delta\nu_B$, corresponding to four cavity free-spectral ranges (FSRs). The long cavity yields a small FSR and relaxes the fabrication precision required to phase match the optical and acoustic fields and stores the large number of photons needed for a low fundamental linewidth. The low-loss (~0.4 dB m⁻¹) Si_3N_4/SiO_2 waveguides support long-lifetime photons that efficiently produce Brillouin optical amplification without the aid of acoustic confinement, leading to long-lifetime photons that continually generate short-lived phonons along the optical waveguide path as illustrated
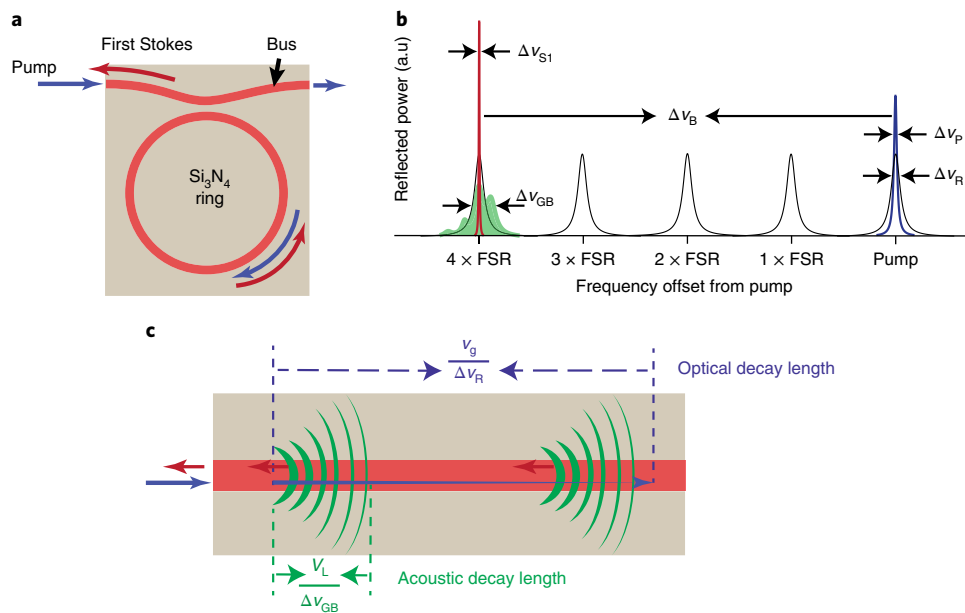
Fig. 2 | Brillouin laser optical guiding, phonon generation and resonant gain. a, Generation of S1 in a Si_3N_4 waveguide Brillouin laser. Pump light injected into the resonator builds to high intensities, leading to spontaneous Brillouin scattering that populates S1. The circulating pump amplifies this incoherent Stokes light, initiating laser oscillation when the round-trip gain compensates for the resonator losses. Brillouin interactions couple counter-propagating optical fields (for example, pump and S1) through travelling sound waves that provide gain for optical amplification. Further increase in the pump power produces successive cascaded-order lasing where distinct wavelengths at the cavity resonances are emitted. **b**, Laser resonator modes, broadened Brillouin gain spectra ($\Delta\nu_{GB}$), and input pump and generated S1 spectra are illustrated in black, green, blue and red, respectively. The Brillouin gain peak is offset from the pump by $\Delta\nu_B = \nu_P - \nu_{S1} \sim 11\,\mathrm{GHz}$, where ν_P is the pump frequency and ν_{S1} is the frequency of S1. The quantities $\Delta\nu_R$, $\Delta\nu_P$ and $\Delta\nu_{S1}$ denote the resonator, pump and S1 linewidths, respectively. **c**, Illustration of phonon generation in an ultralow-loss, high-Q optical resonator without acoustic guiding, where the long optical photon lifetime facilitates continuous generation of short-lived phonons. The large gain spectral width $\Delta\nu_{GB}$ is determined by the fast phonon decay rate. The weak Stokes beam is amplified as it propagates along the waveguide by energy transfer from the pump beam via the phonons. Bulk-like phonons, illustrated as the green diffracting semi-circular waves, have a phonon decay rate three to four times faster than other chip-scale Brillouin lasers and are advantageous for realizing a narrow-linewidth laser. The quantities ν_g and V_L denote the optical group velocity and longitudinal acoustic velocity, respectively.

in Fig. 2c. The Brillouin gain has a large spectral width $\Delta\nu_{GB}$ determined by the fast phonon decay rate. This combination of short phonon lifetime and long photon lifetime suppresses the transfer of pump phase noise to the Brillouin laser emission[21].

A fabricated Si_3N_4 waveguide Brillouin laser chip is shown in the contrast-enhanced image in Fig. 3a. The all-waveguide resonator supports a transverse electric-only mode with an FSR of ~2.72 GHz (see Fig. 3b) and measured full width at half maximum (FWHM) resonance width of 6.87 MHz. The optical resonance width is measured using a radiofrequency calibrated scanning Mach–Zehnder interferometer (MZI)[42] (Fig. 3c) and a cavity ring-down technique[43] (Fig. 3d) that match to within 5%. These calibrated radiofrequency and ring-down measurements correspond to a cold-cavity unloaded Q (Q_U) of ~65.0 million and loaded Q (Q_L) of ~28.2 million (see Fig. 3c). The experimental and simulated Brillouin gain are shown in Fig. 3e, confirming the predicted frequency shift of 10.93 GHz and a predicted gain bandwidth of ~153 MHz. The frequency shift is determined by the material properties of silica since the optical mode propagates predominantly in the oxide waveguide cladding. The high gain bandwidth is attributed to the extremely rapid decay of phonons. Details of the Brillouin gain measurement, simulation and resonator measurements are provided in the Methods.

Lasing power dynamics, linewidth and relative intensity noise.
The laser linewidth, steady-state power dynamics, including lasing threshold and slope efficiency, and RIN are measured using the apparatus shown in Fig. 4a. The laser is pumped with a fibre-coupled 1,550 nm tunable pump that is wavelength-locked slightly off cavity

resonance, using an external phase modulator and Pound–Drever–Hall[44] feedback loop. The optical power spectrum, measured at the reflection port, for the first three Stokes orders is shown in Fig. 4b. The output powers of first (S1) and third (S3) Stokes orders as a function of input pump power, shown in Fig. 4c, clearly shows threshold powers at 14.6 mW and 116.3 mW, respectively, corresponding to threshold densities of 0.52 mW μm^{-2} and 4.18 mW μm^{-2}, respectively. Analytical curves are fit to the experimental power curves using a cascaded-order Brillouin laser theory[26] shown by the dashed lines in Fig. 4c. This theory predicts the steady-state power dynamics by incorporating measured quantities and parameters. Fitting the measured and predicted laser output power, we obtain the bus–ring coupling coefficient (κ^2) and the power coupling from the laser to the optical spectrum analyser (OSA), demonstrating excellent agreement between the analytical and measured steady-state optical powers. The measured cold-cavity resonator characteristics, used to generate the predicted Stokes power curves (cold-cavity fit), agree well until the input pump is increased beyond 150 mW. We attribute this deviation to changes in the resonator characteristics under hot-cavity conditions. At high input pump powers, the intracavity intensity builds to very high values and thermal effects induce changes in cavity parameters including κ^2 and the waveguide group index (n_g). Performing a hot-cavity fit for S1 and S3 where the output power decreases, as shown in Fig. 4c, provides an estimated 5% increase in the external quality factor (Q_{ext}).

Measurement of the 0.72 Hz S1 fundamental linewidth and demonstration of linewidth narrowing as a function of input pump are performed using the experimental setup in Fig. 4a. Linewidth
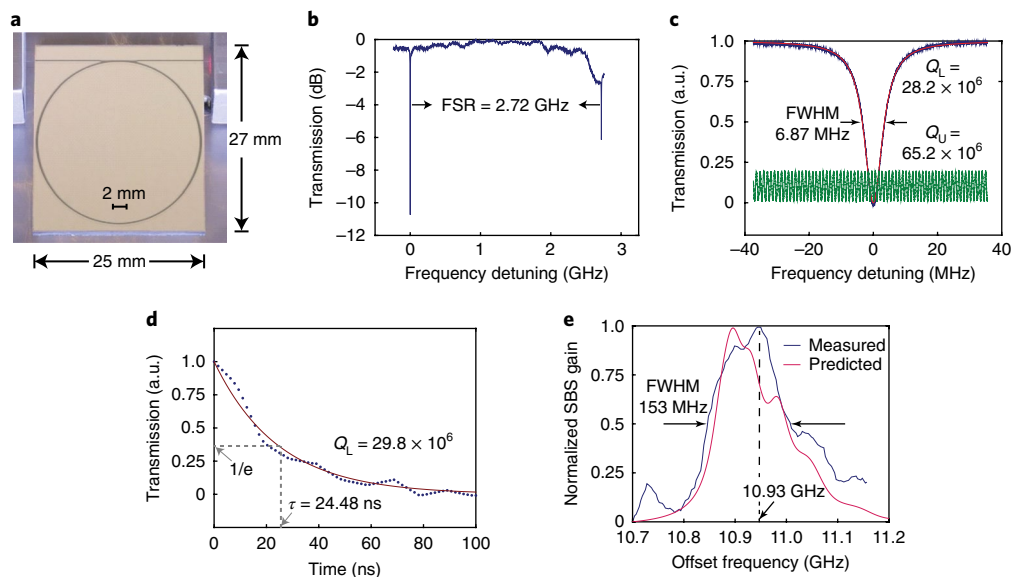
Fig. 3 | Laser resonator cold-cavity characteristics and Brillouin gain measurement and modelling. a, Contrast-enhanced photograph of 27 mm × 25 mm Si_3N_4 waveguide Brillouin laser chip. The resonator length is ~74 mm, with a waveguide group index of 1.478 and optical mode area of 27.83 μm², yielding a cavity mode-volume of ~2.07 × 10⁻¹² m³. Fabrication and optical mode details are provided in the Methods and Supplementary Information. **b**, Resonator transmission spectrum showing a transverse electric-only 2.72 GHz FSR. **c**, Radiofrequency calibrated MZI measurements of resonator transmission FWHM and the calculated loaded and unloaded Q values. The propagation loss and power coupling coefficient are extracted from a Lorentzian profile (red trace) fit to the measured transmission spectra (blue trace). The green trace is the calibrated MZI frequency scale. **d**, Ring-down measurement of the cold-cavity laser resonator results in a cavity ring-down time of 24.48 ns, corresponding to a Q_L of 29.8 million, in agreement with the Q value from radiofrequency calibrated MZI measurement. A first-order exponential decay function (red trace) was fit to the normalized resonator transmission output (dotted blue trace), and the time stamp corresponding to the 1/e point (where e ≈ 2.71828) is extracted as the cavity ring-down time. The cavity-ring down time, τ, and 1/e transmission are indicated by the grey dashed lines. **e**, Measured Brillouin gain spectrum of a Si_3N_4 waveguide spiral using a pump-probe technique (described in Methods) shows an asymmetric spectral profile with an FWHM of ~153 MHz. This gain linewidth is three to four times broader than that of silica wedge resonators[31] and silicon and chalcogenide waveguide Brillouin lasers[32–34].

narrowing is demonstrated by measuring the spectral properties as a function of pump power at the multiple points indicated in Fig. 5a. The linewidth of spontaneous dominated emission ($\Delta\nu_{sp,S1}$), below and at the threshold (points (1) and (2) in Fig. 5a), is directly measured by coherent heterodyne detection of the pump and Stokes output S1 using an electrical spectrum analyser (ESA) (ESA traces (1) and (2) in Fig. 5b). Continued narrowing of the fundamental linewidth is demonstrated with an increase in pump power above the threshold as shown in the frequency-noise plots in Fig. 5c. At the onset of lasing (data points (3)–(9) in Fig. 5a), the fundamental linewidth ($\Delta\nu_{f,S1}$) is measured by evaluating the white-noise floor of the frequency noise measured with a calibrated unbalanced MZI, as shown in the traces in Fig. 5c. Figure 5d summarizes spontaneous and fundamental linewidth measurements, demonstrating significant linewidth narrowing at the onset of lasing. The fundamental linewidth evolves from 142 Hz at the S1 threshold and continues to narrow as shown in traces (4)–(9) in Fig. 5c, reaching 0.72 Hz just below the second Stokes order (S2) threshold. As the S1 white-frequency-noise floor falls below that of the pump (black curve in Fig. 5c), we observe the role that the long photon lifetime relative to the short phonon lifetime plays in suppressing the pump phase diffusion contribution below the Schawlow–Townes contribution. This highlights the advantages of using a large-mode-volume, high-Q, all-waveguide resonator that supports high intracavity intensity to achieve sub-hertz fundamental linewidths.

The S1 RIN is measured using the RIN module of a commercial OEwaves OE4000 laser linewidth/laser phase noise measurement system (setup shown in Fig. 4a). The RIN for S1 is measured at points (9)–(12) in Fig. 5a, and traces are included in the Supplementary Information. We observe RIN reduction as the

S1 power is increased, up to the onset of S2 lasing, where the S1 clamps and the RIN increases as expected from theory[26]. The RIN approaches its minimum value of ~−150 dBc Hz⁻¹ at 40 MHz frequency offset.

Application demonstrations. A photonic integrated Brillouin laser optical gyroscope was demonstrated using the laser chip and discrete front-end gyro components on a rotation table as shown in Fig. 6a. The laser is pumped to emit two Stokes orders. While the gyroscope is at rest under Earth background rotation, the frequency spacing between adjacent optical tones is very close to $f_B = \Delta\nu_B$ (defined earlier in this paper). As the gyroscope rotation is increased, the Sagnac-induced frequency shift results in a relative increase in frequency difference between the counter-propagating first- and second-order Stokes tones, denoted as δν in Fig. 6b. The sign of δν depends on the direction of applied rotation and the value of δν is used to determine the rotation rate. The measured frequency shift δν for an applied rotation rate varying from 0 to 75° s⁻¹ in steps of 25° s⁻¹ is shown in Fig. 6c and demonstrates the required linear operation with a scale factor of 152 Hz per degree per second.

Photonic microwave frequency synthesizers (known as radiofrequency photonic oscillators) produce a microwave signal with phase noise comparable to the best-available electronic oscillators and exhibit frequency stability orders of magnitude better than electronic solutions[45]. Discrete component optical frequency comb generators utilize temperature-stabilized magnesium fluoride (MgF_2) microresonators to achieve record-low phase noise of −170 dBc Hz⁻¹ at 10 MHz offset from the fixed 10 GHz radiofrequency carrier and −90 dBc Hz⁻¹ close-to-carrier at 100 Hz offset[46]. Radiofrequency carrier tunability can be achieved with more complex discrete

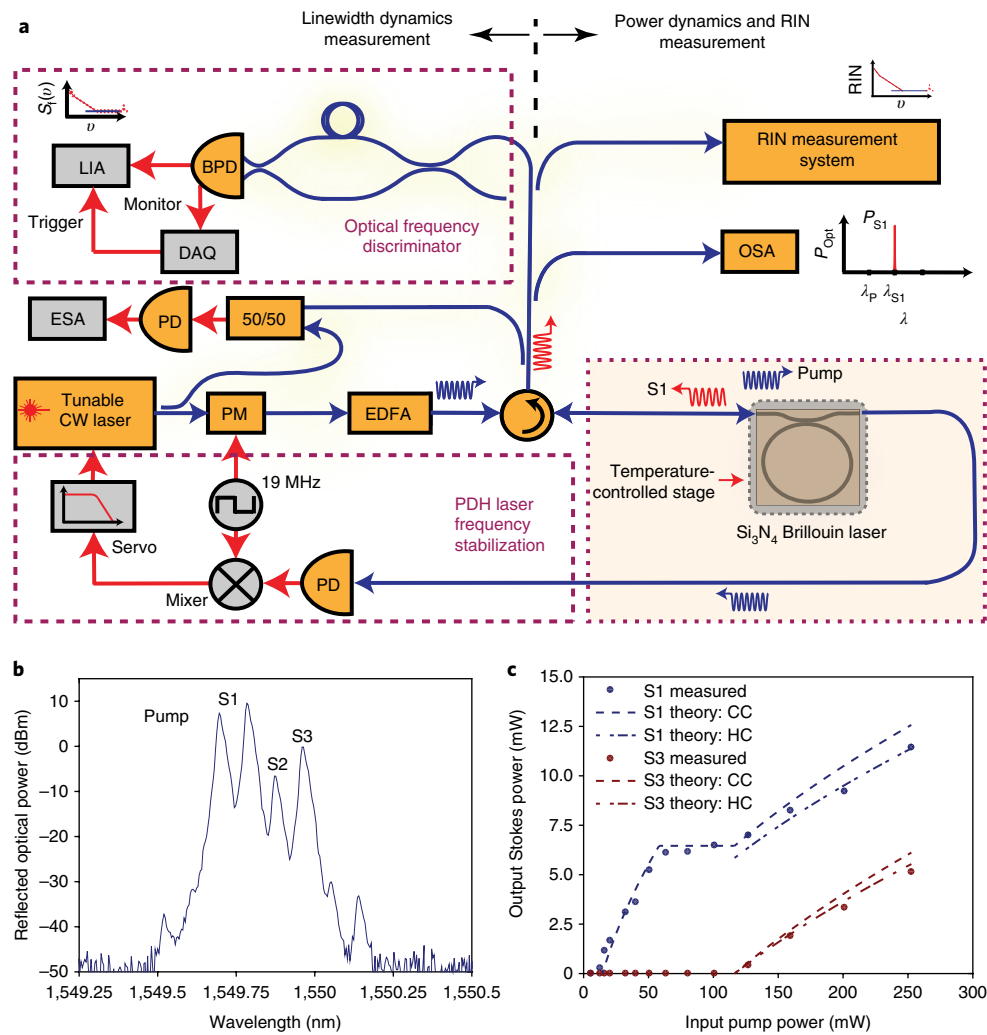**Fig. 4 | Experimental measurement setup and laser threshold, slope efficiency and cascaded-order power dynamics measurement. a**, Experimental setup for measurement of Brillouin laser linewidth, phase noise, RIN and power dynamics. **b**, Measured optical power spectrum at the reflection port for three Stokes orders showing pump and second-order reflection. **c**, Measured cascaded S1 and S3 power dynamics with corresponding analytical curves using cold-cavity (CC) parameters and extraction of hot-cavity (HC) parameters at high pump input powers. The theoretical fits are done using the measured Brillouin gain, the resonator linewidth, the bus–ring coupling coefficient (κ^2) and a calibration factor (β) relating the on-chip power to the power measured on the OSA. By fitting the measured laser output power to the analytical expressions, we obtain the power coupling from the laser to the OSA and κ^2, the only under-constrained parameters. The analytical power evolution curves show excellent agreement for $\beta = 0.35$ and $\kappa^2 = 0.009$. Power of S1 emission clamps at the onset of S2 lasing. 50/50, 3 dB optical power splitter; BPD, balanced photodetector; CW, continuous wave; DAQ, data acquisition controller; EDFA, erbium-doped fibre amplifier; LIA, lock-in amplifier; PD, photodetector; PM, phase modulator; RIN, relative intensity noise; $S_f(\nu)$, single-sided frequency noise in Hz^2 Hz^{-1} where ν is the frequency offset in hertz. The quantities λ and P_{opt} denote the wavelength and optical power. The pump and first Stokes order wavelengths are denoted by λ_P and λ_{S1}, respectively, and P_{S1} is the power of the first Stokes order.

component optoelectronic-optic photonic oscillators that incorporate chip-scale Brillouin waveguides to achieve $<-100\,\mathrm{dBc\,Hz^{-1}}$ at 100 kHz offset as the carrier is tuned from 5 to 40 GHz (ref. [47]). Moving radiofrequency photonic oscillators to the chip scale will lower power consumption, weight and volume, with a trade-off in tunability for today's approaches. The radiofrequency carrier frequency is fixed by the device physical dimensions; however, optical frequency comb-based approaches can provide multiple radiofrequency carrier outputs. Discrete component microresonators utilizing Kerr comb generation produce microwave signals with measured phase noise as low as $-115\,\mathrm{dBc\,Hz^{-1}}$ at 10 kHz frequency offset from a 35 GHz carrier[46]. Low noise microwave frequency generation was reported using a dual-cavity configuration with an etched-silica microresonator Brillouin laser stabilized to a high-Q

microcavity reference with noise performance measuring close to $-90\,\mathrm{dBc\,Hz^{-1}}$ at a frequency offset of 10 kHz from a 21.7 GHz carrier[11]. Creating truly tunable microwave photonic oscillator outputs today is accomplished with multiple photonic chip solutions and adaptation of state-of-the-art dual-comb, self-referenced frequency synthesizers[48].

Here, we demonstrate low single-sided phase noise for a monolithically integrated radiofrequency photonic oscillator, measuring $-84\,\mathrm{dBc\,Hz^{-1}}$ at 10 kHz frequency offset from a 21.8 GHz carrier and a close-to-carrier of $-30\,\mathrm{dBc\,Hz^{-1}}$ at 100 Hz carrier offset. Employing a micro reference cavity and lock circuit[36] has the potential to further suppress the noise at lower frequency offsets towards the fundamental limit. Figure 6d shows the oscillator schematic and the measured phase and frequency noise are shown in Fig. 6e,f with the
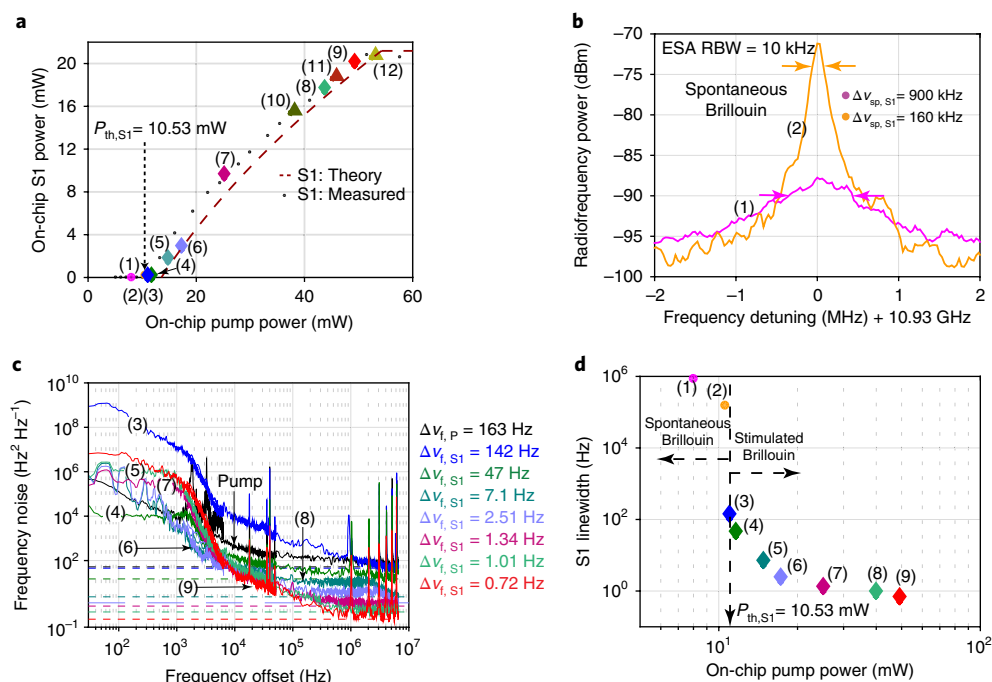
Fig. 5 | Laser linewidth measurement and linewidth narrowing. a, Measured power evolution of S1 at the subthreshold points (1) and (2), corresponding to spontaneous emission spectra curves in **b**. Measurements at the threshold power of 10.53 mW (point (3)) and above threshold (points (4)–(9)) correspond to the frequency-noise curves in **c** and points (9)–(12) correspond to RIN measurements shown in the Supplementary Information. Comparison of theoretical curves to measured data shows agreement with predicted behaviour. **b**, Measurement of subthreshold spontaneous emission spectrum at two pump powers below threshold (corresponding to points (1) and (2)) using a pump–S1 heterodyne beat-note measurement on an ESA with a 10 kHz resolution bandwidth (RBW). **c**, Measurement of the S1 single-sided frequency noise as a function of pump power starting at threshold and above threshold (points (3)–(9)). The dotted lines indicate the far-from-carrier white-frequency-noise level determined by the emission fundamental linewidth. The pump laser frequency noise and its fundamental linewidth are shown in black demonstrating significant pump diffusion phase noise reduction and linewidth narrowing. **d**, Linewidth evolution of S1 from ~1 MHz spontaneous linewidth below threshold to ~0.7 Hz fundamental linewidth above threshold at the onset of S2 lasing. These results demonstrate spontaneous emission bandwidth reduction up to the threshold and the onset of dramatic linewidth reduction at the threshold with continued linewidth narrowing as the pump power is increased.

10 kHz frequency offset denoted. Both the gyro and radiofrequency photonic oscillator applications leverage cancellation of common mode noise sources between the two Stokes orders in the laser resonator during the photo-mixing process.

Applying a cascaded-order Brillouin laser noise dynamics theory[26], the S1 fundamental linewidth can be extracted using the measured single-sided phase of the S1–S3 beat-note (dark blue line in Fig. 6e) and the ratio of their respective optical powers $P_{S1}/P_{S3} = 9.5$ dB (see Fig. 4b). The resulting 0.7 Hz is in good agreement with the expected fundamental linewidth of this laser design. Details of the technique and equations are described in the Methods. The 2.76 Hz upper bound on the fundamental beat-note linewidth $\Delta \nu_{S1-S3}$ at the minimum point in the frequency noise power spectrum as shown in Fig. 6f is justified when assuming that the technical and fundamental sources of noise add in quadrature. Consequently, if technical sources of noise are eliminated, the fundamental beat-note noise can be no larger than the sum of the fundamental noises of individual Stokes orders. By using this relation, requiring only the relative Stokes powers rather than absolute powers, this analysis removes uncertainties in off-chip coupling losses, facet back reflections, and difference between hot- and cold-cavity parameters. In cascaded-order operation, it is important to note that the theoretically predicted phonon-limited linewidth[26] of S1 at pump power close to the threshold of S3 is nearly three times that of the S1 fundamental linewidth at the S2 threshold due to phonon noise contribution from S2.

In Fig. 6f, we compare the frequency noise of the pump and the microwave beat-note, indicating a relative suppression of pump frequency noise. Our measurements reveal regions dominated by

frequency flicker ($1/f$) (region 1), phase flicker (f^1) (region 3) and white frequency noise (region 2 spanning 1–100 kHz). We attribute the features of region 2 to fundamental noise, yielding fundamental frequency noise floor of ~0.9 Hz^2 Hz^{-1}, indicating at least two orders of improvement from the pump laser frequency noise of ~200 Hz^2 Hz^{-1}.

Discussion

In this paper, we report a waveguide integrated sub-hertz fundamental linewidth Brillouin laser. Comprised of an integrated, bus–ring, ultralow-loss Si$_3$N$_4$ waveguide resonator, this laser combines low optical losses, long lifetime photons and short-lived phonons without acoustic waveguiding, a large effective mode area, a large optical mode-volume and a broad Brillouin gain bandwidth, to produce highly coherent laser emission and bring advantages of fibre Brillouin lasers to the chip scale. The long on-chip resonator length and single polarization operation, as well as the broad Brillouin gain bandwidth, reduce sensitivity to fabrication tolerances and minimize dispersion engineering requirements. Consequently, narrow-linewidth Brillouin lasing can be achieved over a broad range of pump wavelengths. By performing radiofrequency beat-note and absolute frequency noise measurements of S1 for pump powers varying from subthreshold to the S2 threshold, we demonstrate significant linewidth narrowing at the onset of lasing and determine the fundamental linewidth of S1 to be ~0.72 Hz for pump powers close to the S2 threshold. Combining the measured single-sided phase noise of the beat-note between S1 and S3 and relative powers of the Stokes orders with cascaded-order Brillouin noise dynamics
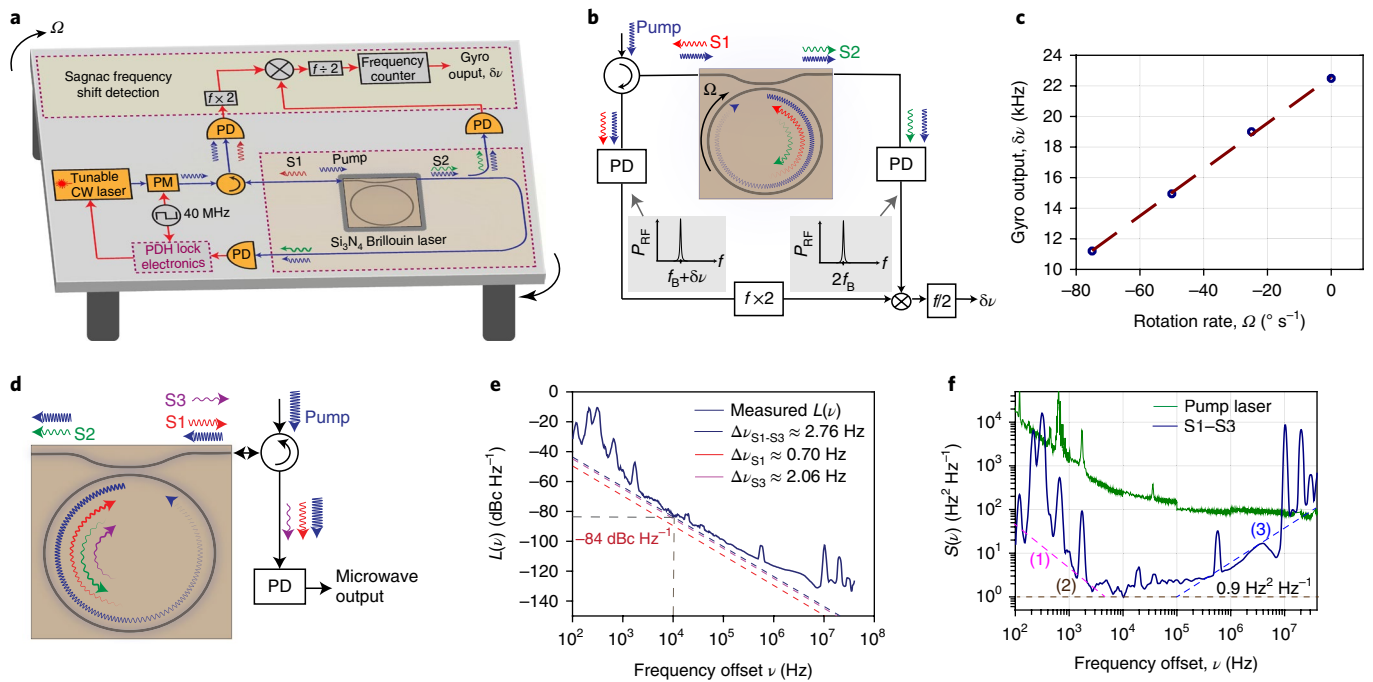
Fig. 6 | Integrated laser optical gyroscope and photonic microwave synthesizer demonstrations. a, Brillouin laser optical gyroscope configured on a rotational stage operated at a rate Ω (° s⁻¹). **b**, Illustration of Sagnac frequency shift ($\delta\nu$) in the Stokes orders circulating in the resonator (pump, blue; S1, red; S2, green). The beat-note between reflected pump and S1 is frequency doubled and mixed with the beat-note between pump and S2 to extract the Sagnac frequency shift. **c**, Measured gyro output for an applied rotation rate varying from 0 to 75° s⁻¹. The measured scale factor is 152 Hz per degree per second. **d**, Photonic microwave synthesizer configured by photo-mixing S1 and S3. **e**, Measured single-sided phase noise of beat-note between S1 and S3 and corresponding theoretical fit lines to indicate the fundamental linewidth of S1 emission. **f**, Comparison of pump frequency noise with S1–S3 beat-note frequency noise. Dashed lines (1), (2) and (3) show the fits to flicker frequency noise, white frequency noise and flicker phase noise regions, respectively. The common noise peaks at 0.6, 1.7 and 3.9 kHz indicate residual transfer of pump phase noise to the Brillouin laser.

theory[26], we confirm the sub-Hz fundamental linewidth of S1 to be ~0.7 Hz. In addition to the low fundamental linewidth, technical noise sources are introduced by the Pound–Drever–Hall locking circuit and other electronics, pump amplitude to Brillouin phase noise conversion, stimulated Brillouin induced RIN, and other close-to-carrier noise sources that contribute to the integral linewidth. The advantage of an all-waveguide design enables integration with other components for cavity control, as is done in fibre Brillouin lasers, to reduce the low -frequency noise components to the quantum and thermal limit[36]. The design allows thermal and stress actuators[37] to be integrated with the resonator cavity itself, as illustrated in Fig. 1a, and is a key aspect in enabling performance normally associated with benchtop Brillouin lasers.

The wafer-scale, foundry-compatible platform makes it possible to create high-performance light sources with reduced size, cost and power consumption as well as integration with a wide variety of Si_3N_4 and silicon photonic waveguide-based integrated active and passive components. Moreover, the waveguide transparency window, from 405 to 2,350 nm, paves the way for narrow-linewidth operation over a broad range of wavebands. The Si_3N_4 platform leads the way to low cost, tunable, highly coherent Brillouin lasers that can be pumped by on-chip, low coherence, heterogeneous III–V/silicon[49] and hybrid III–V/Si_3N_4 (ref. [29]) lasers. The properties of our Brillouin laser make it an ideal source to act as a pump for microresonator-based Kerr frequency combs, as the comb frequency noise is limited by pump laser noise[50]. Si_3N_4 frequency combs pumped with this laser will lead to improved multi-channel WDM compact sources for coherent terabit communications. The spectral purity of this laser can be used to generate low-phase-noise microwave signals directly from multiple Stokes orders or by driving a comb generator.

Looking forward, several design strategies are available to further improve the linewidth and noise performance of this laser. The resonator Q can be engineered by altering the waveguide design and implementing new techniques to further lower waveguide loss. The bus–ring coupling losses can be minimized by increasing the resonator length, and sidewall scattering can be reduced by adjusting the waveguide width and optimizing the post-fabrication annealing process. In addition to design and processing advances, the laser dynamics can be further engineered by manipulating the frequency response of the resonator as well as the Brillouin gain and controlled laser order cascading to adjust the power and coherence of individual Stokes orders. By adopting these strategies, we foresee that resonators with loaded Q more than several hundred million and engineered Brillouin emission will enable unprecedented high-coherence integrated lasers and will be transformative for applications including coherent communications, photonic microwave oscillators, spectroscopy, quantum communications and computing, positional and navigation sensors and atomic clocks.

Online content

Any methods, additional references, Nature Research reporting summaries, source data, statements of data availability and associated accession codes are available at https://doi.org/10.1038/s41566-018-0313-2.

References

1. Kikuchi, K. Fundamentals of coherent optical fiber communications. *J. Lightwave Technol.* **34**, 157–179 (2016).

2. Degen, C. L., Reinhard, F. & Cappellaro, P. Quantum sensing. *Rev. Mod. Phys.* **89**, 035002 (2017).
3. Kitching, J., Knappe, S. & Donley, E. A. Atomic sensors—a review. *IEEE. Sens. J.* **11**, 1749–1758 (2011).
4. Ludlow, A. D., Boyd, M. M., Ye, J., Peik, E. & Schmidt, P. O. Optical atomic clocks. *Rev. Mod. Phys.* **87**, 637–701 (2015).
5. Bartels, A., Oates, C. W., Hollberg, L. & Diddams, S. A. Stabilization of femtosecond laser frequency combs with subhertz residual linewidths. *Opt. Lett.* **29**, 1081–1083 (2004).
6. Young, B. C., Cruz, F. C., Itano, W. M. & Bergquist, J. C. Visible lasers with subhertz linewidths. *Phys. Rev. Lett.* **82**, 3799–3802 (1999).
7. Ludlow, A. D. et al. Sr lattice clock at 1×10^{-16} fractional uncertainty by remote optical evaluation with a Ca clock. *Science* **319**, 1805–1808 (2008).
8. Barwood, G. P. et al. Agreement between two ^{88}Sr^{+} optical clocks to 4 parts in 10^{17}. *Phys. Rev. A.* **89**, 050501(R) (2014).
9. Carlson, D. R. et al. Self-referenced frequency combs using high-efficiency silicon-nitride waveguides. *Opt. Lett.* **42**, 2314–2317 (2017).
10. Diddams, S. A., Ye, J. & Hollberg, L. in *Femtosecond Optical Frequency Comb Technology: Principle, Operation and Applications* (eds Cundiff, S. T. & Ye, J.) 225–262 (Springer, Boston, 2005).
11. Li, J., Lee, H. & Vahala, K. J. Microwave synthesizer using an on-chip Brillouin oscillator. *Nat. Commun.* **4**, 2097 (2013).
12. Li, J., Suh, M.-G. & Vahala, K. Microresonator Brillouin gyroscope. *Optica* **4**, 346–348 (2017).
13. Corbett, J. C. et al. Spanner: Google's globally-distributed database. In *Proc. 10th USENIX Conference on Operating Systems Design and Implementation* 251–264 (USENIX Association, 2012).
14. Hu, H. et al. Single-source chip-based frequency comb enabling extreme parallel data transmission. *Nat. Photon.* **12**, 469–473 (2018).
15. Perin, J. K., Shastri, A. & Kahn, J. M. Design of low-power DSP-free coherent receivers for data center links. *J. Lightwave Technol.* **35**, 4650–4662 (2017).
16. Olsson, S. L. et al. Probabilistically shaped PDM 4096-QAM transmission over up to 200 km of fiber using standard intradyne detection. *Opt. Express* **26**, 4522–4530 (2018).
17. *Cisco Visual Networking Index: Forecast and Methodology*, 2016–2021 (Cisco, 2017); https://www.cisco.com/c/en/us/solutions/collateral/service-provider/visual-networking-index-vni/complete-white-paper-c11-481360.html
18. Andrae A. Total Consumer Power Consumption Forecast (researchgate.net, 2017); https://www.researchgate.net/publication/320225452_Total_Consumer_Power_Consumption_Forecast
19. Hill, K. O., Kawasaki, B. S. & Johnson, D. C. cw Brillouin laser. *Appl. Phys. Lett.* **28**, 608–609 (1976).
20. Jihong, G. et al. Highly stable low-noise Brillouin fiber laser with ultranarrow spectral linewidth. *IEEE Photon. Technol. Lett.* **18**, 1813–1815 (2006).
21. Debut, A., Randoux, S. & Zemmouri, J. Linewidth narrowing in Brillouin lasers: theoretical analysis. *Phys. Rev. A.* **62**, 023803 (2000).
22. Woodward, R. I., Kelleher, E. J., Popov, S. V. & Taylor, J. R. Stimulated Brillouin scattering of visible light in small-core photonic crystal fibers. *Opt. Lett.* **39**, 2330–2333 (2014).
23. Smith, S. P., Zarinetchi, F. & Ezekiel, S. Narrow-linewidth stimulated Brillouin fiber laser and applications. *Opt. Lett.* **16**, 393–395 (1991).
24. Loh, W. et al. A microrod-resonator Brillouin laser with 240 Hz absolute linewidth. *New J. Phys.* **18**, 045001 (2016).
25. Geng, J. & Jiang, S. Pump-to-Stokes transfer of relative intensity noise in Brillouin fiber ring lasers. *Opt. Lett.* **32**, 11–13 (2007).
26. Behunin, R. O., Otterstrom, N. T., Rakich, P. T., Gundavarapu, S. & Blumenthal, D. J. Fundamental noise dynamics in cascaded-order Brillouin lasers. *Phys. Rev. A.* **98**, 023832 (2018).
27. Mooradian, A. Laser linewidth. *Phys. Today* **38**, 42–48 (1985).
28. Santis, C., Vilenchik, Y., Yariv, A., Satyan, N. & Rakuljic, G. Sub-kHz quantum linewidth semiconductor laser on silicon chip. In *CLEO: 2015 Postdeadline Paper Digest* JTh5A.7 (OSA, 2015).
29. Fan, Y. et al. 290 Hz intrinsic linewidth from an integrated optical chip-based widely tunable InP-Si$_3$N$_4$ hybrid laser. In *CLEO: 2017 Paper Digest* JTh5C.9 (OSA, 2017).
30. Grudinin, I. S., Matsko, A. B. & Maleki, L. Brillouin lasing with a CaF$_2$ whispering gallery mode resonator. *Phys. Rev. Lett.* **102**, 043902 (2009).
31. Lee, H. et al. Chemically etched ultrahigh-Q wedge-resonator on a silicon chip. *Nat. Photon.* **6**, 369–373 (2012).
32. Otterstrom, N. T., Behunin, R. O., Kittlaus, E. A., Wang, Z. & Rakich, P. T. A silicon Brillouin laser. *Science* **360**, 1113–1116 (2018).
33. Morrison, B. et al. Compact Brillouin devices through hybrid integration on silicon. *Optica* **4**, 847–847 (2017).
34. Kabakova, I. V. et al. Narrow linewidth Brillouin laser based on chalcogenide photonic chip. *Opt. Lett.* **38**, 3208–3211 (2013).
35. Bauters, J. F. et al. Planar waveguides with less than 0.1 dB/m propagation loss fabricated with wafer bonding. *Opt. Express* **19**, 24090–24101 (2011).
36. Loh, W. et al. Dual-microcavity narrow-linewidth Brillouin laser. *Optica* **2**, 225–232 (2015).
37. Blumenthal, D. J. et al. Silicon nitride in silicon photonics. *Proc. IEEE* **106**, 2209–2231 (2018).
38. Herr, T. et al. Temporal solitons in optical microresonators. *Nat. Photon.* **8**, 145–152 (2013).
39. Roeloffzen, C. G. H. et al. Low-loss Si$_3$N$_4$ TriPleX optical waveguides: technology and applications overview. *IEEE J. Sel. Top. Quantum Electron.* **24**, 4400321 (2018).
40. Spencer D. T. et al. Integrated single and multi-layer Si$_3$N$_4$ platform for ultralow loss propagation and small bending radii. In *Optical Fiber Communication Conference* (pp. Th1A-2) (OSA, 2014).
41. Huffman, T. A. et al. Integrated resonators in an ultralow loss Si$_3$N$_4$/SiO$_2$ platform for multifunction applications. *IEEE J. Sel. Top. Quantum Electron.* **24**, 5900209 (2018).
42. Li, J., Lee, H., Yang, K. Y. & Vahala, K. J. Sideband spectroscopy and dispersion measurement in microcavities. *Opt. Express* **20**, 26337–26344 (2012).
43. Armani, D. K., Kippenberg, T. J., Spillane, S. M. & Vahala, K. J. Ultra-high-Q toroid microcavity on a chip. *Nature* **421**, 925–928 (2003).
44. Drever, R. W. P. et al. Laser phase and frequency stabilization using an optical resonator. *Appl. Phys. B* **31**, 97–105 (1983).
45. Fortier, T. M. et al. Generation of ultrastable microwaves via optical frequency division. *Nat. Photon.* **5**, 425–429 (2011).
46. Liang, W. et al. High spectral purity Kerr frequency comb radio frequency photonic oscillator. *Nat. Commun.* **6**, 7957 (2015).
47. Merklein, M. et al. Widely tunable, low phase noise microwave source based on a photonic chip. *Opt. Lett.* **41**, 4633–4636 (2016).
48. Spencer, D. T. et al. An optical-frequency synthesizer using integrated photonics. *Nature* **557**, 81–85 (2018).
49. Tran, M. et al. Ultra-low-loss silicon waveguides for heterogeneously integrated silicon/III–V photonics. *Appl. Sci.* **8**, 1139 (2018).
50. Liao, P. et al. Dependence of a microresonator Kerr frequency comb on the pump linewidth. *Opt. Lett.* **42**, 779–782 (2017).

Author contributions

S.G., G.M.B., R.B., P.T.R. and D.J.B. prepared the manuscript. S.G., G.M.B., M.P. and J.W. contributed equally to performing the system, lasing and noise measurements. T.H., D.B. and J.N. contributed to the Si$_3$N$_4$ integrated laser fabrication. M.P., S.G., D.B., P.T.R., R.B., J.N., K.D.N., M.S. and D.J.B. contributed to the laser design. R.B., P.T.R., M.P., T.Q., S.G. and K.D.N. contributed to the simulation and modelling. G.M.B., C.P., N.C. and S.G. built the radiofrequency calibrated Mach–Zehnder interferometer and ring-down systems and measured the laser resonator properties. S.G., G.M.B., C.P., M.P. and J.W. performed Brillouin gain measurements. All authors contributed to analysing simulated and experimental results. D.J.B., K.D.N., P.T.R. and M.S. supervised and led the scientific collaboration.

Competing interests

The authors declare no competing interests.

Additional information

Supplementary information is available for this paper at https://doi.org/10.1038/s41566-018-0313-2.

Reprints and permissions information is available at www.nature.com/reprints.

Correspondence and requests for materials should be addressed to D.J.B.

Publisher's note: Springer Nature remains neutral with regard to jurisdictional claims in published maps and institutional affiliations.

Methods

Fabrication methods. A 40-nm-thick stoichiometric Si_3N_4 film was deposited using low-pressure chemical vapour deposition on a 100 mm diameter silicon wafer with a pre-grown 15 μm thermal oxide. The wafer was spun with standard deep ultraviolet (DUV) anti-reflective and photoresist layers and then patterned using an ASML PAS 5500/300 DUV stepper. The anti-reflective coating was etched with a reactive ion etch PlasmaTherm etch tool. The resist was used as an etch mask to realize high-aspect-ratio waveguide core by anisotropically dry etching the Si_3N_4 film in a Panasonic E640 inductively coupled plasma etcher in a CHF_3/CF_4/O_2 chemistry. The resulting byproducts from this etch were then ashed with a Panasonic E626I inductively coupled plasma tool in an O_2 atmosphere before stripping the resist by sonicating in a hot N-methyl-2-pyrrolidone solution and rinsing in isopropanol. The anti-reflective coating and other organic impurities were removed by dipping the wafer in a freshly prepared, standard piranha solution heated at 100 °C. An additional plasma clean using a Gasonics Aura 2000-LL Downstream asher tool helped remove leftover resist and other organic materials. The device features were inspected with a JEOL 7600F field emission scanning electron microscope and the RMS sidewall roughness was measured using a Dimension 3100 atomic force microscope to be lower than 3 nm. A 6-μm-thick oxide was deposited using plasma-enhanced chemical vapour deposition with tetraethyl orthosilicate as a precursor followed by a two-step anneal at 1,050 °C for 7 h, and 1,150 °C for 2 h. The fabrication process flow is illustrated in the Supplementary Information.

Gain simulation methods. Material thin films and Si_3N_4 waveguides were characterized to extract the optical and acoustic parameters used to populate full vectorial Brillouin gain simulations. The refractive index, material density and Young's modulus of thermally grown oxide, low-pressure chemical vapour-deposited nitride and plasma-enhanced chemical vapour-deposited oxide films on silicon wafers were measured using optical ellipsometry, X-ray reflectometry and nano-indentation techniques, respectively. These values were used to simulate the position, shape and amplitude of the Brillouin gain spectra by constructing fully three-dimensional finite element method models of the waveguides yielding a gain peak frequency shift of 10.92 GHz. This frequency shift is expected as the optical mode is confined mostly in the oxide. The simulated gain spectrum exhibits a high degree of skewness towards higher frequencies due to acoustic waves that couple into a portion of the bulk-like continuum. Further details about the Brillouin gain simulation in a non-acoustic guiding Si_3N_4 waveguide are given in the Supplementary Information.

Waveguide loss and coupler measurements. Additional device characteristics that are necessary for an optimized laser resonator include waveguide loss and the bus–ring coupling coefficient. For waveguide loss measurements, a 5 m spiral with a waveguide design identical to that of the resonator was measured using optical backscatter reflectometry yielding a propagation loss of 1.14 dB m⁻¹. The spiral consists of 42 turns stitched between four DUV masks with a total of 168 stitches and includes a central s-bend where it reverses spiralling direction. This s-bend has the smallest radius in the design of 11.83 mm. For the high-Q resonators, the coupling coefficients were calibrated using test structures with a straight waveguide coupled to a curved waveguide with a bend radius of 11.83 mm and a gap distance that was varied across devices from 1.5 to 5.5 μm. For the resonators used in this study, we chose the gap distances of 5.42 μm and 6.0 μm based on measured and simulated power coupling ratios of 0.5% and 0.25%, respectively.

Brillouin gain measurement. Experimental measurement of the Brillouin gain spectra and coefficient of Si_3N_4 waveguide spirals was performed using a standard pump-probe technique (setup shown in the Supplementary Information). Two tunable lasers were directed through circulators and polarization controllers, then coupled into a temperature-stabilized 5-m-long segment of waveguide spiral from opposite ends. The silica fibre pigtail of the circulator that couples pump laser into the spiral was shortened and spliced to a segment of a highly nonlinear single-mode Nufern UHNA3 fibre that has a Brillouin gain peak spectrally isolated from that of the waveguide. This allowed us to isolate the contribution of probe gain within the silica fibre from that of the integrated waveguides. The pump was amplified with an erbium-doped fibre amplifier and the difference in optical frequency between the two lasers was swept through the simulated Brillouin peak frequency shift. The frequency-dependent gain was determined from the probe input/output power ratio for on-chip pump powers varying from ~200 to 600 mW and pump-probe frequency detuning of 10.7 to 11.1 GHz. The effective 2.7843 m length of spiral is calculated by taking into account the measured 1.14 dB m⁻¹ loss and yields a peak Brillouin gain coefficient of 0.10 ± 0.009 m⁻¹ W⁻¹ at a frequency detuning of ~10.93 GHz. This measured gain is in strong agreement with our simulations providing confidence in our understanding of the underlying gain properties.

Laser resonator design. The Brillouin resonator FSR was designed to be ¼ the measured Brillouin frequency shift ($\Omega = 2\pi 10.93$ GHz), which is possible due to the low optical waveguide loss enabling a large high-Q resonator. This design guarantees that the Brillouin-active optical mode is within 1.366 GHz from resonance, relaxing fabrication precision of the resonator size. Two different

resonators with physical lengths of 74.3 mm and 74.1 mm corresponding to FSRs of 2.728 GHz = (10.91 GHz)/4 and 2.732 GHz = (10.93 GHz)/4, respectively, were fabricated. The resonator bend radii, 11.83 mm and 11.80 mm, respectively, were chosen to be larger than the critical bend loss limit (~10 mm) for this waveguide design. An FSR of 2.72 GHz was measured for the 74.33-mm-long resonator using a single-sideband tunable swept optical source. This value differs by only 8 MHz from the target FSR, which combined with the large ~153 MHz Brillouin gain bandwidth, highlights the fabrication robustness of this design.

FSR and Q measurement. A 200 m unbalanced fibre-based MZI was used as a reference frequency spectrum to accurately measure the resonator Q (ref. [42]). A single-sideband swept laser source was used to calibrate the MZI FSR. The single-sideband swept source was generated by passing an intensity modulated laser through two cascaded fibre Bragg gratings to suppress the carrier and upper sideband. The filtered lower sideband was passed through the MZI and the carrier modulation frequency was swept in time using a microwave synthesizer and the interferometer FSR was measured by monitoring the transmitted power on a synchronized oscilloscope. The frequency spacing between fringes of the intensity output was measured to be 1.07 ± 0.0146 MHz. By simultaneously scanning the laser frequency through both the MZI and device under test, the MZI fringe spacing (FSR) provides a radiofrequency calibrated frequency reference for accurate evaluation of resonator Q factors. A standard cavity ring-down technique[43] was used to confirm the radiofrequency calibrated MZI measurements. For this measurement, a fibre laser was frequency swept around a resonator resonance by applying a triangular voltage input to laser piezoelectric transducer control. Further, a 50% duty cycle, 10 kHz square wave was applied to the intensity modulator with fast switching response (<10 ns) to serve as the gating signal. The gating signal is synchronized to set the input power to zero when the input laser is at ring resonance and the optical power inside the cavity discharges with an exponential decay. This 'ring-down' decay time (τ) was measured by monitoring the transmission port output on an oscilloscope and used to evaluate the loaded quality factor of the resonator ($Q_L = \omega\tau$). The ring-down time and Q_L of a representative resonator were measured to be 24.48 ns and 29.2 million.

Fundamental linewidth measurement. We measured the frequency noise and fundamental linewidth of our Brillouin laser based on an optical frequency discriminator using a fibre-based unbalanced MZI (UMZI) and a balanced photodetector. The relation between power spectral density of the detector output, $S_{out}(\nu)$ in (V² Hz⁻¹), frequency noise of the laser, $S_f(\nu)$ in (Hz² Hz⁻¹), and the fundamental linewidth of the laser, $\Delta\nu_{S1}$ in Hz, is given by:

$$S_f(\nu) = S_{out}(\nu)\left(\frac{\nu}{\sin(\pi\nu\tau_D)V_{PP}}\right)^2 \tag{1}$$

$$\Delta\nu_{S1} = \pi S_w \tag{2}$$

where τ_D is the optical delay of the UMZI, ν is the frequency offset, V_{PP} is the peak–peak voltage of the detector output, and S_w is the value of frequency noise where $S_f(\nu)$ is flat (indicates white-frequency-noise-dominated region).

The Brillouin laser output from the reflection port of the circulator is directed to an acoustically isolated, 200 m fibre delay-based UMZI with a FSR of 1.03 MHz. The two outputs of the UMZI are connected to a switchable gain, balanced photodetector (Thorlabs PDB450C) with a bandwidth of 45 MHz to reduce the impact of intensity fluctuations in the detector output. The power spectral density ($S_{out}(\nu)$) of the detector output is measured over several decades of frequency offsets (sampling rates: 13 kSa s⁻¹, 103 kSa s⁻¹, 3.3 kSa s⁻¹, 26 MSa s⁻¹, 53 MSa s⁻¹) using a lock-in amplifier (Zurich instruments HF2LI 50 MHz). The monitor port of the detector connected to a National Instruments data acquisition controller (NI USB 6259) is programmed to trigger the lock-in amplifier at the quadrature operating point of the UMZI. The single-sided fast Fourier transform data are averaged over 10 traces using an exponential moving average filter and a Hann window is applied to reduce spectral leakage. The measured decade-wise power spectral density outputs are stitched together to determine $S_{out}(\nu)$ and converted to $S_f(\nu)$ using equation (1). The Stokes fundamental linewidth, $\Delta\nu_{S1}$, is calculated using equation (2) from the flat portion of the measured frequency noise S_w.

We use a second technique to determine and confirm the sub-Hz fundamental laser linewidth by combining the measured phase noise power spectrum of the beat-note between S1 and S3, the emitted laser powers, and results from cascaded-order Brillouin laser theory[26]. For the mth Stokes order, the fundamental linewidth $\Delta\nu_m$ is given by

$$\Delta\nu_m = \frac{1}{4\pi N_m}[\gamma_m(N_m^{th} + n_{m-1}^{th} + 1)]$$
$$[+ 2\mu_m N_{m+1}(n_m^{th} + n_{m-1}^{th} + 1)] \tag{3}$$

Here, γ_m, μ_m, N_m and N_m^{th} are the respective decay rate, Brillouin amplification rate per pump photon, and coherent intracavity and thermal photon numbers,

all defined for the mth order. The thermal occupation number, n_m^{th}, is defined for the phonon mode mediating Brillouin scattering between the $(m-1)$th and mth orders. The variables μ_m and N_m can be expressed in terms of more familiar quantities by using the following relations:

$$\mu_m = \frac{\hbar \omega_m c^2}{2 n_g^2 L} \left(\frac{g_{Bm}}{A_{\text{eff}}} \right) \quad N_m = \frac{n_g L}{\hbar \omega_m c \, \kappa^2} P_m \tag{4}$$

where ω_m, g_{Bm}, and P_m are the respective angular frequency, bulk Brillouin gain coefficient and emitted power of the mth mode and κ^2 is the bus–ring power coupling factor. Other parameters are the resonator length (L), the effective opto-acoustic overlap area (A_{eff}), and c and $\hbar$, the speed of light and the reduced Planck constant, respectively. The fundamental linewidth is dominated by the thermomechanical noise arising from the thermal phonon number n_m^{th} (~570 at room temperature). Since our laser has a relatively large Brillouin gain bandwidth (fast decay rate), the transferred pump noise is compressed by a factor[21] of $(1 + \Gamma/\gamma_m)^2$, where Γ is the decay rate of the acoustic mode, ensuring that the linewidth component that dominates other all-waveguide designs[32,34], is negligible compared with the fundamental linewidth given by equation (3).

The S1 fundamental linewidth was also extracted by combining the measured beat-note phase noise of S1 and S3, resonator Q factors and cascaded Brillouin laser theory. The beat-note single-sided phase noise power spectrum $L(\nu)$, between S1 and S3, is measured using the setup shown in Fig. 4a. The region of the phase noise power spectrum determined by fundamental sources of noise, is related to the beat-note linewidth by[26]:

$$L(\nu) = \frac{\Delta \nu_{S1-S3}}{2\pi\nu^2} \tag{5}$$

where $\Delta \nu_{S1-S3}$ is the linewidth of the S1, S3 photomixed beat-note on a detector and ν is the frequency offset from this beat-note. It should be noted that this beat-note measurement suppresses noise sources common to both S1 and S3.

The fundamental linewidth $\Delta \nu_{S1-S3}$ can be expressed as the sum of the individual linewidths of the participating Stokes tones[26] as $\Delta \nu_{S1-S3} = \Delta \nu_{S1} + \Delta \nu_{S3}$ and additionally yields the dependence of these linewidths on the ratio of the emitted powers P_{S1} and P_{S3}. For third-order cascading, the individual Stokes order linewidths are directly related to the measured value for $\Delta \nu_{S1-S3}$ and the relative optical powers through the following relations[26]:

$$\Delta \nu_{S3} \approx \frac{\Delta \nu_{S1-S3}}{\left(1 + \frac{3P_{S3}}{P_{S1}} \right)} \quad \text{and} \quad \Delta \nu_{S1} \approx \frac{\Delta \nu_{S1-S3}}{\left(1 + \frac{P_{S1}}{3P_{S3}} \right)} \tag{6}$$

Data availability

The data that support the plots within this paper and other finding of this study are available from the corresponding author on reasonable request.